Research Article

Environmental Chemistry and Safety
DOI: 10.26599/ECS.2025.9600052
2025, 1, 9600052

Two-dimensional CoS/Co-MOF Composite Electrocatalyst for Efficient Oxygen Evolution Reaction

Manqi Liu[1], Baiming Liang[1], Yu Liang[1], Ying Peng[1], Yuxuan Lin[1], Zhikuan Wang[1], Yu Wang[1], Zemei Tan[1], Yulu Yang[1], Hongxia Xi[2], Jingjing Li[1]*, and Chongxiong Duan[1]*

[1]School of Materials and Engineering, Foshan University, Foshan, 528231, China

[2]School of Chemistry and Chemical Engineering, South China University of Technology, Guangzhou, 510640, China

Abstract: The oxygen evolution reaction (OER) is the key anodic reaction in water electrolysis for hydrogen production. Herein, a novel two-dimensional (2D) CoS/Co-MOF composite electrocatalyst was successfully synthesized using a post-synthesis method. The as-synthesized 2D CoS/Co-MOF composite employed as an OER electrocatalyst exhibits an exceptionally low overpotential of 327 mV at a current density of 100 mA cm^{-2}, considerably outperforming most reported transition metal sulfide catalysts (e.g., NiS/MOFs: 368 mV, Co_9S_8@MoS_2/Co-MOFs: 350 mV). Furthermore, the resulting CoS/Co-MOF OER electrocatalyst demonstrates exceptional stability, maintaining stable catalytic activity after 20 h of constant-current operation and exhibiting minimal degradation after 30 days of air exposure. In addition, a systematic investigation of key parameters (e.g., the thioacetamide (TAA) content and reaction temperature) was conducted to identify the optimal process conditions. Moreover, the catalytic mechanism of CoS/Co-MOF electrocatalyst was further elucidated based on density functional theory (DFT) calculations. These results reveal that the introduction of CoS can modulate the d-band centre of the CoS/Co-MOF, thereby optimizing adsorption free energy and reducing the overpotential. This synergy between the structure and optimized synthesis parameters advances the sustainable development of high-performance OER electrocatalysts. This work offers a feasible method for designing efficient and durable electrocatalysts that can facilitate large-scale applications of water electrolysis for hydrogen production.

Key words: Metal-organic frameworks (MOFs); oxygen evolution reaction (OER); electrocatalysts; post-synthesis method.

Citation: Liu M Q, Liang B M, Liang Y, et al. Two-dimensional CoS/Co-MOF Composite Electrocatalyst for Efficient Oxygen Evolution Reaction. *Environmental Chemistry and Safety*, 2025, 1, 9600052. https://doi.org/10.26599/ECS.2025.9600052

1. Introduction

Hydrogen is an important energy carrier that plays an essential role in achieving carbon neutrality owing to its zero-carbon emissions and high energy density. Approximately 96% of the global hydrogen production depends on fossil fuel reforming, generating 10–12 tonnes of CO_2 per ton of hydrogen[1]. Green hydrogen production using proton exchange membrane water electrolysis is a sustainable alternative. However, its industrial scalability is primarily limited by the intrinsic challenges of the oxygen evolution reaction (OER). This reaction is crucial in water electrolysis because it is the main anodic process that supplies the protons and electrons required for hydrogen production at the cathode. Notably, OER is a kinetically sluggish four-electron transfer process that requires overcoming a high thermodynamic energy barrier (theoretical potential: 1.23 V)[2], leading to considerable overpotential and substantial energy loss.

Recently, various transition-metal-based electrocatalysts, such as oxides, hydroxides and sulfide/phosphide derivatives, have been extensively explored to accelerate the sluggish OER kinetics. Specifically, transition-metal oxides and hydroxides are inexpensive and stable, yet their catalytic activity is limited by intrinsically low conductivity, insufficient exposure of active sites, and the difficulty of precisely tailoring their local coordination environments[3, 4]; Although single-atom catalysts offer maximized atomic utilization, their metal centers are difficult to anchor at high density and tend to migrate or aggregate under oxidative potentials[5]. Overall, the catalytic performance of these materials is fundamentally constrained by restricted structural tunability and limited control over the electronic microenvironment of active sites.

Metal-organic frameworks (MOFs) are a highly promising catalyst platform due to their intrinsically ordered porous architectures, abundant active sites, and tailorable coordination environments. Their crystalline architectures, constructed from metal nodes and organic linkers, provide intrinsically high surface areas and fully accessible active sites, in contrast to the buried or partially exposed sites in dense inorganic materials. More importantly, the coordination environment around the metal centers in MOFs can be precisely tuned through linker chemistry and metal-ligand design, enabling electronic and structural modulation that is difficult to achieve in oxides, hydroxides, or sulfide/phosphide catalysts[6]. These features make MOFs highly attractive for constructing well-defined and tunable catalytic sites for the OER. However, the intrinsic defects (e.g., inherent chemical instability, poor mass trans-

Correspondence to: Li J J, jjli@fosu.edu.cn; Duan C X, cechxduan@fosu.edu.cn

Received: September 30, 2025; Revised: November 25, 2025; Accepted: December 8, 2025

port properties) of MOFs result in a considerable discrepancy between their theoretical and actual performance[7-9]. For example, metal-ligand bonds of MOFs are susceptible to hydrolysis and breakage in alkaline electrolytes, leading to structural collapse[10]. In addition, the domain-limited pore environment of MOFs is dominated by micropores, hindering the contact between the electrolyte and approximately 80% of the active sites, leading to a substantial decrease in the apparent activity[11]. Liu et al.[12] developed atomically precise catalysts with increased hydrolytic stability of less than 100 h. However, their bond-breaking rate constants ($k \geqslant 0.01$ min^{-1}) failed to meet the industrial requirements. Chen et al.[13]designed a 2D-layered MOF nanostructure with numerous binding sites; however, it suffered from the limited domain of the micropores, which restricted the utilization of active sites to approximately 80%. Therefore, bridging this performance gap remains a key challenge. Thus, the objective of this work is to minimize the difference between the theoretical and practical values through structural and electronic modulation.

Herein, a post-synthesis method was developed to transform a Co-MOF precursor into a novel 2D CoS/Co-MOF electrocatalyst. The composite was processed into ultra-thin nanosheets via a post-synthesis method, considerably enhancing the charge transfer and active site accessibility and resulting in a 6.2-fold increase in electrochemically active surface area (ECSA) and a low overpotential of 327 mV at 100 mA cm^{-2}. Furthermore, the formation of Co-S covalent bonding enhances the composite structural stability and optimizes intermediate adsorption. This was confirmed through density functional theory (DFT) calculations, which indicate a reduction in the energy barrier of the rate-determining step. Crucially, the MOF framework is retained, and outstanding OER performance is achieved, with a low overpotential and exceptional durability of over 500 h. This study provides a scalable and efficient strategy for green hydrogen production.

2. Experimental

2.1. Synthesis of Co-MOFs

In a typical synthesis, a mixture of 6 mL anhydrous ethanol and 10 mL dimethylacetamide (DMAC) was prepared. Then, 0.3 mmol of cobalt nitrate hexahydrate and 0.3 mmol of biphenyldicarboxylic acid were added to the mixture. The resulting solution was stirred for 60 min, transferred to an autoclave, sealed, and reacted at 150°C for 3 h. After natural cooling to room temperature, the product was centrifugally washed three times with a mixed solution of 10 mL of anhydrous ethanol and 10 mL of DMAC. Finally, the solid was vacuum-dried at 50°C for 12 h, and it is denoted as Co-MOFs[14].

2.2. Synthesis of CoS/Co-MOF composite

The CoS/Co-MOF composite was prepared via a post-synthesis method, and the detailed procedure is illustrated in Fig. 1. First, 50 mg of Co-MOFs and 450 mg of thioacetamide (TAA) were added to a mixture of 6 mL anhydrous ethanol and 10 mL DMAC. After stirring for 60 min, the mixture was transferred to an autoclave, sealed, and reacted at 150°C for 3 h. After natural cooling to room temperature, the product was centrifugally washed three times with a mixture of 10 mL of anhydrous ethanol and 10 mL of DMAC. Finally, the obtained product was vacuum-dried at 50°C for 12 h, and it is labeled as CoS/Co-MOF composite.

2.3. Characterization

2.3.1. Characterization

The crystal structure was identified by XRD. SEM and TEM revealed the sheet-like morphology and detailed microstructure. XPS confirmed the presence and chemical states of Co, S, C, N, and O. FTIR spectra (4000-500 cm^{-1}) further verified the organic linkers. BET surface area and pore structure were measured by N_2 adsorption–desorption on an ASAP 2460. AFM (Bruker Dimension Icon) was used to measure the thickness and surface roughness.

2.3.2. Electrochemical measurements

All electrochemical measurements were carried out in 1 M KOH using a typical three-electrode configuration. OER activity was benchmarked by LSV, and Tafel slopes were extracted from the polarization curves. Stability was assessed by multi-hour chronopotentiometry at constant current. ECSA was derived from double-layer capacitance measured by CV in a non-Faradaic region. EIS revealed the charge-transfer resistance at the electrode/electrolyte interface.

2.4. Calculation

All DFT calculations were performed using the Vienna Ab initio Simulation Package (VASP). The exchange-correlation effects were described by the Perdew-Burke-Ernzerhof (PBE) functional within the generalized gradient approximation (GGA). Core-electron interactions were treated with the projector augmented wave (PAW) method, and the valence electrons were expanded in a plane-wave basis set with a cutoff energy of 500 eV. The convergence criteria were set to 10-5 eV for electronic self-consistency and 0.02 eV/Å for ionic relaxation. Because of the large model size, Brillouin zone sampling was limited to the Gamma point using a 1×1×1 Monkhorst-Pack k-mesh.

The Gibbs free energy change (ΔG) reflects how strongly the OER intermediates bind to the active sites. This value is closely related to the electronic structure of the catalyst. For each elementary step, ΔG was calculated using the following equation:

$$\Delta G = \Delta E + \Delta EZPE - T\Delta S + \Delta Geleph + \Delta Gph$$

The electron energy difference, ΔE, was derived from DFT

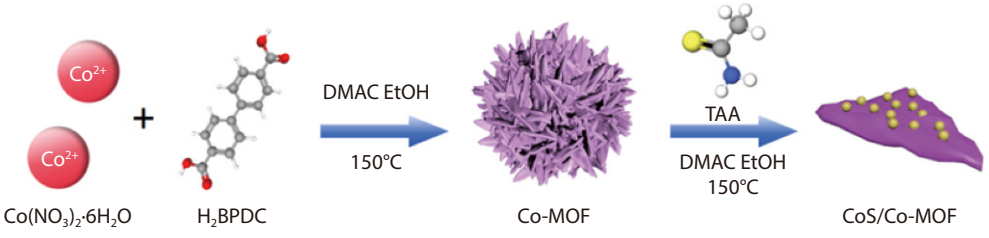

Fig. 1. Schematic illustration of the synthetic route for CoS/Co-MOF composite.

calculations. Changes in zero-point energy and entropy, denoted as $\Delta EZPE$ and ΔS, respectively, were determined from vibrational frequency analysis. For gas-phase molecules, entropy corrections were taken from standard reference databases. The reaction temperature T was set to 298.15 K. The free energy contribution includes a potential-dependent term incorporating n, the number of electrons transferred, e, the elementary charge, and U, the electrode potential. An additional correction for pH, $\Delta G\_(pH)$, was applied using the relation $\Delta G\_(pH) = k\_B\ T \times pH \times ln(10)$, where k_B is the Boltzmann constant[15-17].

3. Results and discussion

3.1. Crystal structure and morphology analysis

To analyze the effect of sulfidation on crystal structure and chemical bonding transformations, XRD and FTIR characterizations were initially conducted. As shown in Fig. 2a, the XRD pattern reveals that the as-synthesized CoS/Co-MOF composite retains characteristic Co-MOF peaks at 12.1°, 13.6°, 18.3°, 29.2°, and 30.8°, confirming the partial inheritance of MOF structural advantages such as high specific surface area and abundant active sites. Conversely, peak intensities at 6.1°, 12.4°, 14.1°, 15.3°, and 18.8° are significantly attenuated[18], indicating that the partial dissociation of the Co-MOF backbone structure induced by sulfidation. Moreover, FTIR analyses are performed to probe the evolution of chemical bonding. As shown in Fig. 2b, the peak at 3169 cm^{-1} is attributed to N–H stretching vibrations[19], while those at 1080 and 1010 cm^{-1} are assigned to S=O vibrations, confirming the involvement of TAA in ligand substitution. Furthermore, the band observes at 526 cm^{-1} corresponds to S-S stretching, and signals at 831 and 663 cm^{-1} are ascribed to C-S bending vibrations[20, 21]. These features indicate the formation of a metal-sulfur covalent network. These spectroscopic evidences verify the structural transformation identified by XRD and establish the bonding foundation for the material's charge transport capacity (EIS: 57 Ω) and active site exposure (ECSA: 86.6 mF cm^{-2}).

The morphological evolution of Co-MOFs and CoS/Co-MOF composite was revealed by SEM. As shown in Fig. 3a, the as-synthesized CoS/Co-MOF composite exhibits a granular morphology distinct from Co-MOFs, with particle size substantially reduced from 1 μm to 200 nm. This structural transformation stems from sulfur atoms released during TAA decomposition reacting with metal sites of Co-MOFs under high temperature and pressure conditions, concurrently inducing dimensional reduction and specific surface area enhancement of 2D nanosheets while promoting the formation of metal sulfides such as CoS[22]. To analyze spatial distribution-morphology correlations, the energy-dispersive X-ray spectroscopy (EDS) result confirms homogeneous dispersion of S and Co elements without aggregation (Fig. 3e), verifying uniform loading of high-density sulfur atoms on the Co-MOF substrate and successfully constructing CoS/Co-MOF composite. Compared with the 3D flower cluster shape of Co-MOFs, the CoS/Co-MOF composite exhibits a randomly distributed 2D nanosheet structure (Fig. S1), which contributes to its enhanced electrocatalytic performance. This ultrathin configuration (atomic-layer thickness) exposes nearly all atoms as active sites[23, 24], thus enhancing specific surface area and site density. This 2D nanosheet structure confers dual advantages, including (i) electron transport is facilitated by the 2D lamellae of the CoS/Co-MOF composite that provides a topological basis for exposing active sites, and (ii) stacking defects are suppressed, leading to enhanced oxidation resistance and electrochemical stability[25].

To further validate the ultrathin 2D nanosheet configuration of the CoS/Co-MOF composite, AFM was conducted to quantitatively assess the thickness and nanoscale roughness of the samples, as shown in Fig. 4. The AFM height profiles reveal distinct thickness variations under different synthesis conditions, with measured feature heights of 6.135, 9.699, 7.870, and 8.137 nm, respectively. These results confirm that the CoS/Co-MOF composite maintains a nanoscale thickness, consistent with the SEM-observed sheet-like morphology. Notably, Fig. 4c-d exhibit a higher density of uniformly distributed nanostructures, suggesting improved structural homogeneity and potentially higher exposure of catalytically active surface atoms. The combination of SEM and AFM results indicates that the sulfur-induced structural reconstruction not only refines the lateral dimensions of the nanosheets but also regulates their vertical thickness, thereby providing a favorable topography for enhanced electrocatalytic activity.

In addition, the textural properties of the samples were evaluated by N_2 adsorption-desorption measurements. As shown in Fig. S2 and Table S1, the pristine Co-MOFs exhibit a typical IV isotherm with a larger adsorption capacity, corresponding to a BET surface area of 19.31 $m^2\ g^{-1}$ and a pore volume of 0.11 $cm^3\ g^{-1}$. After the incorporation of CoS, the BET surface area decreases to 13.19 $m^2\ g^{-1}$ and the pore volume decreases

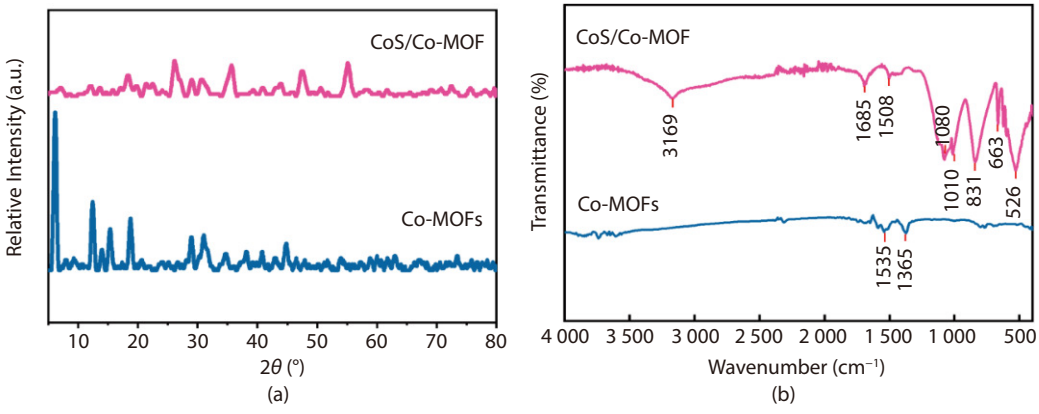

Fig. 2. (a) XRD patterns and (b) FTIR spectra of Co-MOFs and CoS/Co-MOF composite.

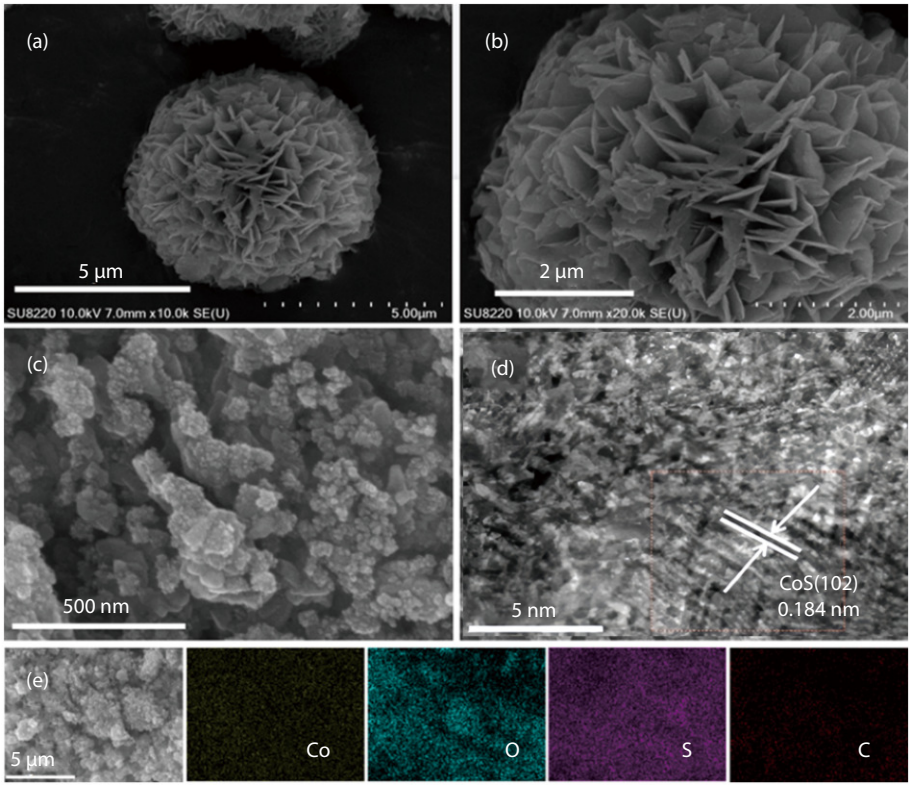

Fig. 3. (a-b) SEM images of Co-MOFs; (c) SEM image of the CoS/Co-MOF composite; (d) HRTEM image showing lattice fringes with an interplanar spacing of 0.184 nm, corresponding to the (102) crystal plane of CoS; and (e) elemental mapping of the composite (Co, O, S, C).

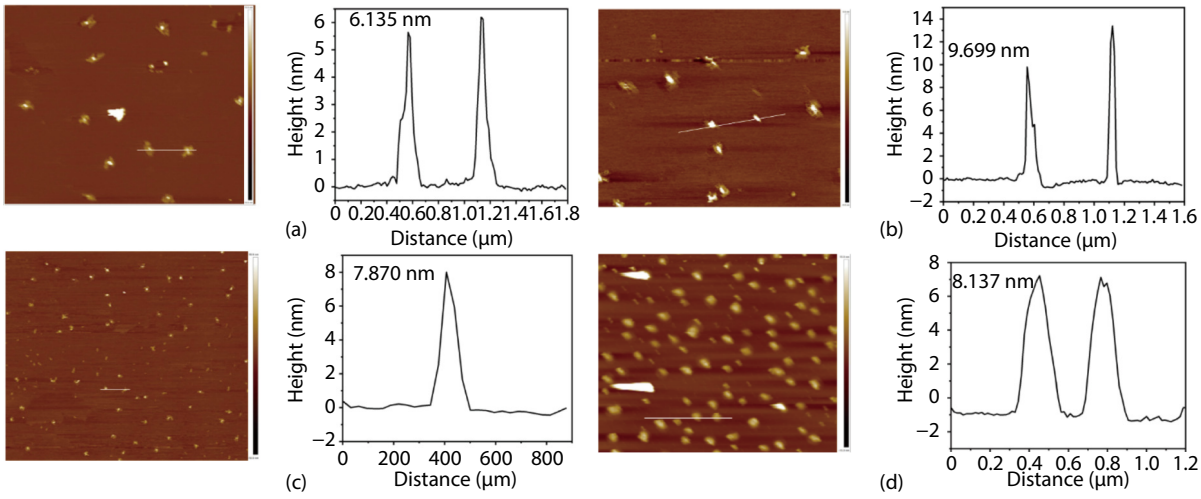

Fig. 4. AFM surface morphology and height profiles of the samples (a-d), showing nanoscale sheet-like features with measured thicknesses of 6.135, 9.699, 7.870, and 8.137 nm, respectively.

to 0.06 $cm^3 g^{-1}$, accompanied by a slight contraction of the average pore size (from 22.3 to 18.9 nm). Such reductions can be attributed to the partial occupation and surface coverage of MOF pores by CoS nanoparticles rather than structural collapse, which is fully consistent with the SEM, TEM, and XRD results. Notably, the composite still preserves well-defined mesoporous channels, providing efficient ion-diffusion pathways that support the improved electrochemical performance discussed below.

3.2. Chemical composition and bonding analysis

To further elucidate the electronic structure and valence states of constituent elements of CoS/Co-MOF composite, XPS spectra of CoS/Co-MOF composite are shown in Fig. 5 (the full survey spectrum is shown in Fig. S3). Fig. 5a displays the C 1s fine scan for CoS/Co-MOF composite, deconvoluted into C=O (288.82 eV), C-OH (287.23 eV), C-S (285.99 eV), and C=C (284.80 eV) species, indicating the emergence of C-S bonds concurrent with C-Co bond disappearance, which signifies the MOF-to-sulfide transition. As shown in the O 1s fine scan of Fig. 5b, the persistent peaks of C=O (531.94 eV) and C-O (533.23 eV) confirm the retention of the Co-MOF organic framework during sulfidation[26]. Simultaneously, the absence of Co-O bonds stems from TAA competing with organic ligands for metal coordination sites during vulcanization, ultimately causing Co-O bond cleavage and metal sulfide formation[27]. Fig. 5c presents the high-resolution Co 2p XPS spectra for CoS/Co-MOF composite, revealing that cobalt primarily exists as Co^{2+} (797.29 eV, 781.28

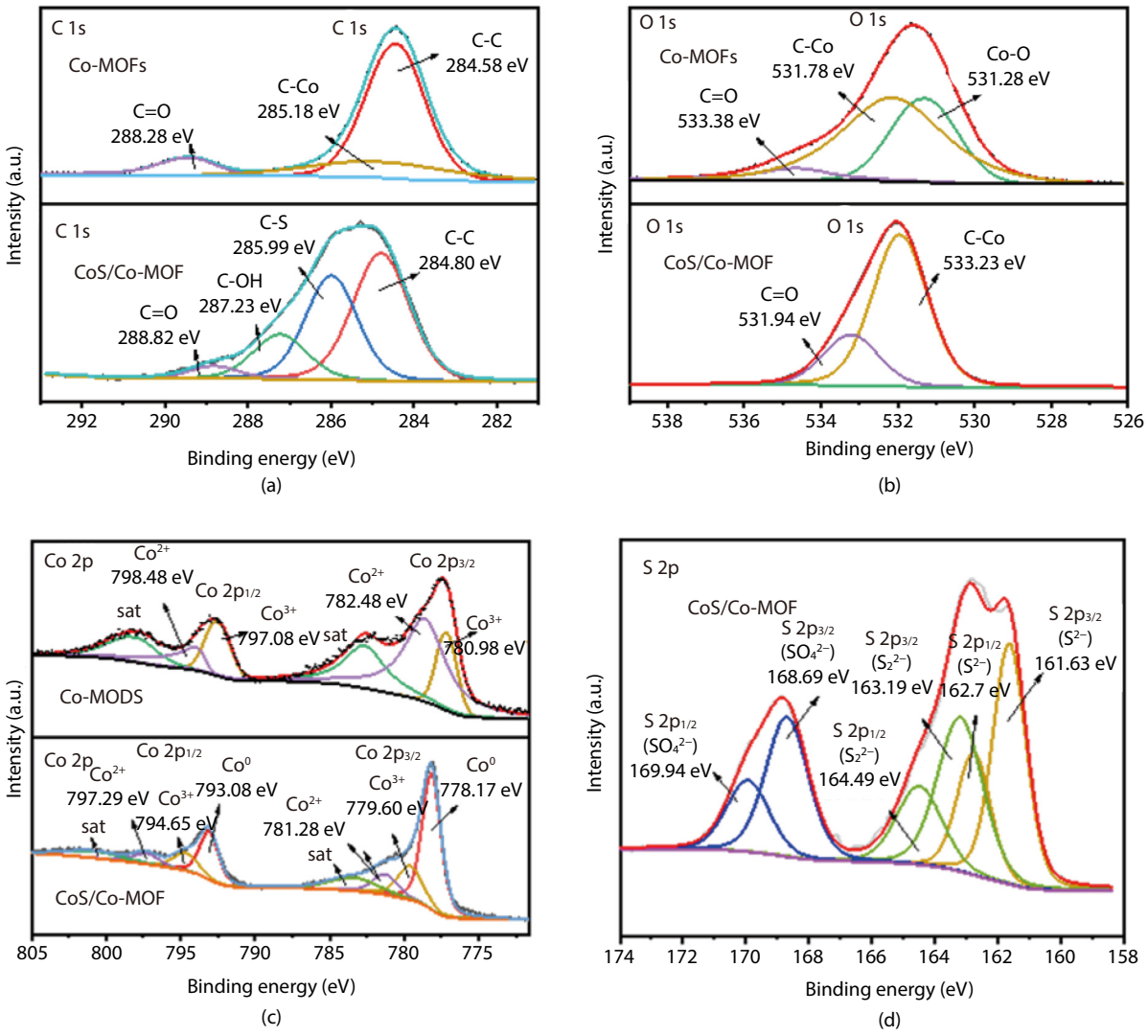

Fig. 5. High-resolution XPS spectra of (a) C 1s, (b) O 1s, (c) Co 2p, and (d) S 2p for Co-MOFs and CoS/Co-MOF composite. Characteristic peaks and corresponding chemical states are labeled.

eV), Co^{3+} (794.65 eV, 779.60 eV), and Co^0 (793.08 eV, 778.17 eV), with the latter two peaks attributed to Co-Co bonds[28]. Notably, the presence of metallic cobalt (Co^0) can be attributed to the in situ partial reduction of cobalt ions by thioacetamide, which acted as a mild reducing agent under the solvothermal conditions, a phenomenon supported by previous literature[29-31]. Fig. 5d displays the S 2p fine scan, the sulfur element transforms into other species such as SO_4^{2-} (169.94 eV, 168.69 eV), S_2^{2-} (164.49 eV, 163.19 eV), and S^{2-} (162.76 eV, 161.63 eV). The peak of 163.19 eV corresponds to Co-S bonding, while the 162.76 eV peak originates from surface low-coordinated S ions, aligning with literature reports and confirming transition metal sulfide formation where S_2^{2-} represents disulfide bonds[32, 33]. Collectively, Co-S (161.63 eV) and S-S (163.19 eV) bonds enhance intermediate adsorption and facilitate electron transfer, further verifying the formation of sulfide. In addition, surface SO_4^{2-} results from sulfide air oxidation[26]. As reported in the literature[34, 35], these species significantly boost OER activity by optimizing the electronic structure.

3.3. Electrocatalytic oxygen evolution performance

Electrochemical performance of composite-loaded glassy carbon electrodes was evaluated in a three-electrode system within 1 M KOH electrolyte. Compared with Co-MOFs (414 mV), the as-synthesized CoS/Co-MOF composite exhibits a substantially lower overpotential (274 mV at 20 mA cm^{-2}), as shown in Fig. 6a. This performance enhancement primarily can be attributed to the formation of sulfide-induced lamellar structure that provides abundant active sites and facilitates charge transfer[32]. Notably, CoS/Co-MOF composite shows lower overpotential than reported transition metal sulfide catalysts (Table 1), further confirming its potential as an efficient OER catalyst. In addition, to further benchmark the catalytic activity, the performance of CoS/Co-MOF composite was compared with the widely accepted noble-metal benchmark catalyst RuO_2. Commercial RuO_2 typically requires an overpotential of ≈ 300–320 mV at 20 mA cm^{-2} in 1 M KOH, as commonly reported for OER benchmarking[36-39]. This value is higher than that of the CoS/Co-MOF composite (274 mV at 20 mA cm^{-2}), indicating that the composite even approaches or surpasses the activity of RuO_2 under identical evaluation conditions. Considering that RuO_2 is one of the most active OER catalysts but suffers from high cost and limited stability, the superior intrinsic activity of the CoS/Co-MOF composite underscores its practical potential as a cost-effective and competitive alternative to

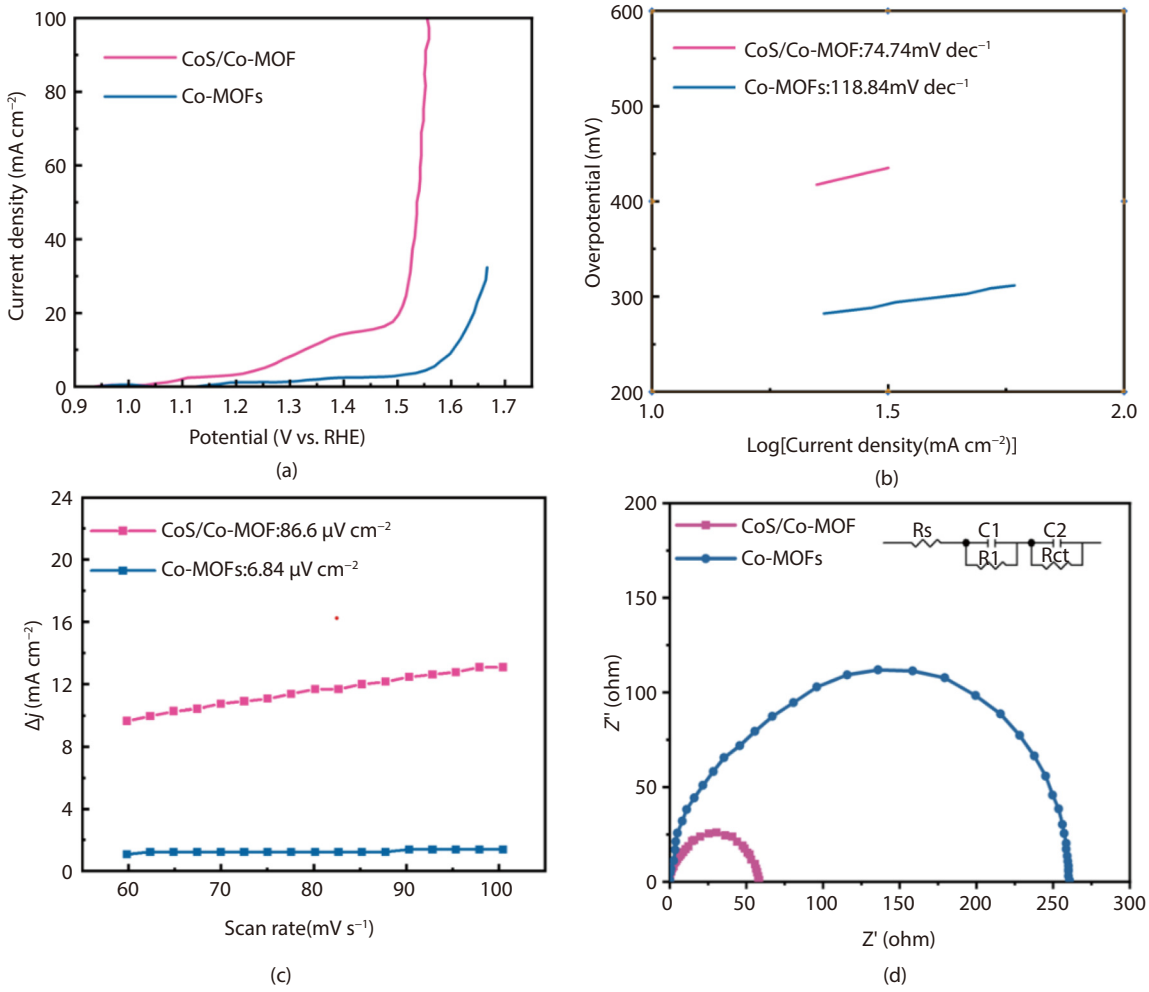

Fig. 6. (a) LSV curves, (b) Tafel plots derived from (a), (c) ECSA estimated from Cdl, (d) Nyquist plots from EIS (corresponding key parameters are labeled).

Table 1. Comparative analysis of OER performance between CoS/Co-MOF composite and homologous transition metal sulfides electrocatalysts.

Sample	Overpotential (mV @ 10 mA cm^{-2})	Tafel slope (mV dec^{-1})	Stability (h @ mA cm^{-2})	Ref.
$CoNi_xS_y$/NCP	280	71	10 @ 1.52 V	[40]
$NiCo_2S_4$@CC	370 (100 mA cm^{-2})	95.76	20 @ 1.60 V	[32]
Co_9S_8/NSCNFs-850	302	54	10 @ 1.55 V	[20]
h-Co_xS_y	320	98	18 @ 10	[41]
Co_9S_8-NSC@Mo_2C	293	59.7	20 @ 300 mV	[26]
Ni-Ni_3S_2@carbon nanoplates	284.7	56	/	[24]
Co/C_9S_8@NSOC-800	373	80	/	[42]
CoS@C/10Graphene	450	/	4.17 @ 10 (0.1M KOH)	[43]
NiCoS/$Ti_3C_2T_x$	365	58.2	6 @ 10	[44]
Co-MOFs	377	118.84	18 @ 10	This work
CoS/CO-MOF	274 (20 mA cm^{-2})	74.74	20 @ 10	This work

noble-metal oxides.

The OER kinetics were further investigated by Tafel slope analysis. A smaller Tafel slope means faster reaction kinetics, because the overpotential increases more slowly with rising current density[45]. As shown in Fig. 6b, the CoS/Co-MOF composite (74.74 mV dec^{-1}) exhibits a lower Tafel slope than Co-MOFs (118.84 mV dec^{-1}) at 1.5 log (current density), manifesting faster OER kinetics. Through the construction of CV curves at varied scan rates, Cdl was calculated. Given Cdl's proportionality to ECSA[46], its value can be used to estimate the active site density. As shown in Fig. 6c, the Cdl value of CoS/Co-MOF is 86.6 μF cm^{-2}, which is much higher than that of the Co-MOF before sulfidation (only 6.84 μF cm^{-2}). Such a large increase in Cdl suggests that far more active sites are exposed in the composite, leading to better intrinsic OER activity. This observation agrees well with previous reports from Yang's group.[33].

The OER performance depends on both ECSA and charge transfer resistance, with the latter being particularly critical for evaluating the intrinsic activity of the catalyst. EIS measurements were employed to investigate ion and charge transfer processes at the catalyst–electrolyte interface. The Nyquist plots exhibited excellent fitting quality, enabling extraction of

quantitative electrochemical parameters that accurately reflect the intrinsic charge-transfer characteristics of the catalyst. The semicircle diameter corresponds to charge transfer resistance (Rct), with lower Rct values indicating higher charge transfer efficiency. As shown in the Fig. 6d, the obtained CoS/Co-MOF composite exhibits a markedly smaller impedance arc, indicating a lower charge-transfer resistance than that of the unsulfurized Co-MOF (257 Ω). This corresponds to a much lower charge-transfer resistance of 57 Ω. The faster charge transfer kinetics can be attributed to the inherent metallic conductivity of CoS, which effectively promotes electron transfer[33]. Collectively, the electrochemical evidence establishes that the performance superiority of CoS/Co-MOF composite originates from three synergistic microstructural properties, including (i) 2D nanosheet morphology enhances ECSA to 86.6 mF cm^{-2} through maximal active site exposure[24], directly enabling the low overpotential of 274 mV at 20 mA cm^{-2}; (ii) Strong Co-S covalent bonding (XPS: 161.6 eV) optimizes charge transport pathways, reduces Rct to 57 Ω[33], and accelerates OER kinetics (Tafel slope: 74.74 mV dec^{-1}); and (iii) the S–S vibration (FTIR: 526 cm^{-1}) indicates additional bonding interactions that help stabilize the framework, as evidenced by the higher decomposition temperature of the composite in TGA (>380°C, Fig. S4)[47].

Electrochemical stability is an important indicator of catalyst performance. Chronopotentiometric tests were carried out at 10 mA cm^{-2} to evaluate the stability. As shown in Fig. 7a, the CoS/Co-MOF electrode operates steadily for more than 20 h, and a slight improvement in performance can even be observed during the test. In comparison, the Co-MOF electrode remains stable for only about 18 h. This enhanced durability mainly comes from the 2D nanosheet structure, which helps release mechanical strain, and from the stronger Co-S bonds that are more resistant to alkaline corrosion. In addition, the FTIR spectra before and after the stability test show clear changes in the carboxylate and Co-S bands (Fig. S5), indicating structural adjustments during long-term operation. Environmental stability testing further validates practicality: after 30-day ambient exposure, CoS/Co-MOF composite shows minimal LSV curve variation (Fig. 7b), with 100 mA cm^{-2} overpotential increasing only from 327 mV to 350 mV. As shown in Fig. S6, the CoS/Co-MOF was characterized by SEM after the stability test. The stacked, grass-like morphology enhances the material's electrochemical stability by providing buffer space, which comes at the cost of partial electrocatalytic activity and conductivity.

3.4. Electrochemical performances enhancement via parameter optimization

The structural properties of CoS/Co-MOF composite can be precisely tuned through the TAA dosage, and reaction parameters, thereby significantly modulating OER electrocatalytic performance (synthesis details and naming conventions are provided in the SI)[48]. Specifically, TAA concentration critically determines both MOF-to-sulfide conversion extent and active site density[49]. Concurrently, reaction parameters (e.g., temperature and time) control the formation of crystalline defects and the development of conductive networks[50]. These factors synergize with intrinsic material activity and mass-transfer efficiency to enable the systematic optimization of OER performance.

3.4.1. The effect of TAA addition on OER performance

TAA dosage is a critical parameter for controlling MOF-to-transition metal sulfide conversion during CoS/Co-MOF composite preparation. As shown in Fig. S7, the catalytic activity of CoS/Co-MOF composite demonstrates a volcano-shaped trend versus TAA dosage, peaking at 450 mg. This optimal addition maximizes retention of MOF precursor structural advantages (high specific surface area, abundant active sites) while enabling sufficient transition metal sulfide formation. Conversely, excessive TAA (500 mg) completely destroys the MOF backbone, blocks active sites, eliminates MOF-derived porosity advantages, and reduces charge transfer rates-severely compromising OER performance. Insufficient TAA (400 mg) causes incomplete sulfidation, preventing adequate transition metal sulfide active site formation. Both non-optimal conditions detrimentally impact composite OER performance[22].

The XRD patterns in Fig. S8 further confirm the important role of TAA dosage. When the optimal amount of TAA (450 mg) was used, the diffraction peaks were very weak and broad, indicating that CoS existed in a highly dispersed and partly amorphous state and was uniformly distributed on the

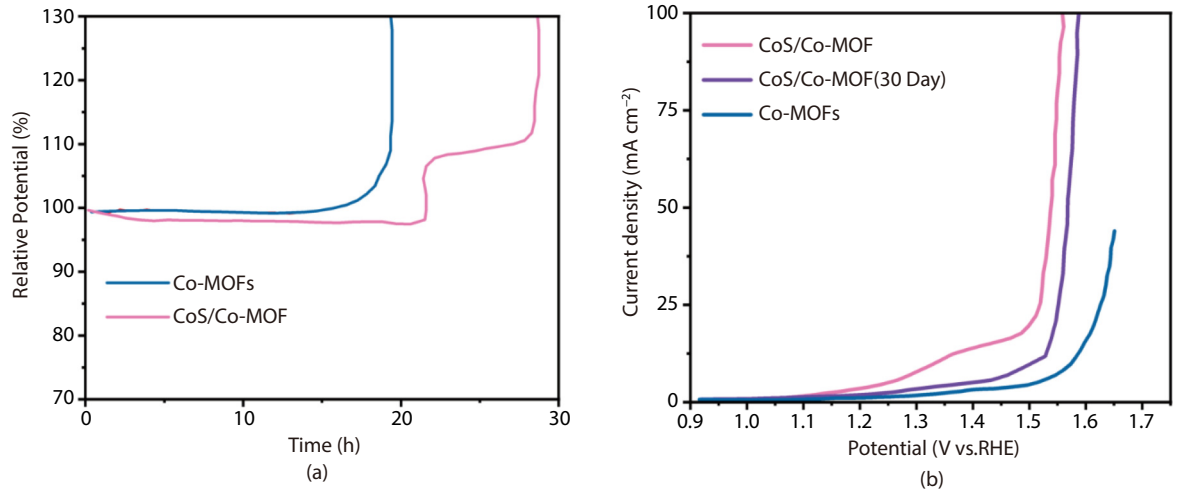

Fig. 7. (a) Stability tests of Co-MOFs and CoS/Co-MOF composite at a current density of 10 mA cm^{-2}, and (b) stability test of Co-MOFs and CoS/Co-MOF composite under open exposure conditions.

Co-MOF framework. In contrast, when too much TAA (500 mg) was added, several sharp peaks appeared in the XRD pattern. This means large crystalline CoS particles formed and the MOF framework collapsed seriously, which explains the obvious drop in catalytic activity. On the other hand, when TAA was insufficient (400 mg), strong diffraction peaks from the remaining precursor were still observed, showing that the sulfidation reaction was not complete. All these results clearly explain the volcano-type trend of OER activity with changing TAA amount and prove that 450 mg is indeed the best condition to obtain the most suitable phase and nanostructure for oxygen evolution catalysis.

3.4.2. The impact of reaction temperature and time on OER performance

As shown in Fig. S9, raising the temperature from 125 to 150°C improves all key performance metrics. The overpotential decreases by 21.7% (from 382 to 327 mV), the Tafel slope decreases by 32.2% (from 100.47 to 68.13 mV dec^{-1}), and the ECSA increases by 46.2% (from 59.22 to 86.6 μF cm^{-2}). These improvements suggest that moderate heating enhances vulcanization without compromising structural order. However, the overpotential sharply increases to 441 mV (34.9% higher than 150°C) at 175°C while ECSA dramatically decreases to 15.62 μF cm^{-2} (82% reduction from 150°C), confirming high-temperature MOF backbone collapse and active site destruction. As shown in Fig. S10, reaction time exhibits non-monotonic effects, with optimal performance at 3 h (327 mV, 86.6 μF cm^{-2}), while 2 h (358 mV, 72.44 μF cm^{-2}) and 4 h (338 mV, 44.1 μF cm^{-2}) samples suffer from under-sulfidation and over-etching respectively. Thus, the optimal condition of 150°C for 3 h is identified. Under the optimal conditions, maximum vulcanization is achieved while the integrity of the MOF pore channels is preserved. This leads to a synergistic optimization of both active site density and charge transfer efficiency.

In addition, the XRD patterns corroborate these electrochemical trends. As shown in Fig. S11, the sample synthesized at 150°C for 3 h exhibits the sharpest and most intense diffraction peaks, indicating the highest crystallinity and well-preserved Co-MOF framework. In contrast, samples prepared at 125°C or with shorter reaction time (2 h) show slightly broadened peaks associated with incomplete sulfidation, while those obtained at 175°C or prolonged reaction time (4 h) display markedly weakened and broadened peaks, confirming partial collapse of the MOF backbone. These results further validate that 150°C for 3 h represents the optimal balance between structural integrity and sulfidation degree.

3.5. Deciphering the catalytic enhancement mechanism by DFT calculations

Systematic DFT calculations were conducted to elucidate the optimization mechanism of the Co-S bond in CoS/Co-MOF composite with regard to the kinetics of the OER. By constructing models of the crystal plane of CoS (102), the interface of organic ligand, and the heterojunction structure of CoS/Co-MOF composite, the changes in adsorption free energy for each elementary step in the four-electron pathway of the OER were systematically calculated.

$$^{*} + H_2O \rightarrow {}^{*}OH + H^{+} + e^{-} \quad (1)$$

$$^{*}OH \rightarrow {}^{*}O + H^{+} + e^{-} \quad (2)$$

$$^{*}O + H_2O \rightarrow {}^{*}OOH + H^{+} + e^{-} \quad (3)$$

$$^{*}OOH \rightarrow {}^{*} + O_2 + H^{+} + e^{-} \quad (4)$$

Compared with pure Co-MOFs, the interface of CoS/Co-MOF composite substantially reduces the energy required for the rate-determining step (step 3, oxygen-oxygen bond formation), as illustrated in the free energy diagram in Fig. 8a. Specifically, the Gibbs free energy change for this step is 1.8 eV for pure Co-MOFs, while it decreases to 1.47 eV for the CoS/Co-MOF composite. This reduction can be attributed to the electronic structure rearrangement induced by the Co-S covalent bond, which shifts the d-band center of Co at the composite interface to a lower energy level of 1.23 eV. This optimization significantly tunes the adsorption strength of oxygen-containing intermediates (particularly *OOH), thereby lowering the reaction energy barrier of the rate-determining step.

The DFT calculations reveal that the downward shift of the d-band center induced by CoS significantly reduces the activation barrier for O-O bond formation, thereby decreasing the sensitivity of the reaction rate to overpotential variations. As illustrated in Fig. 8b, the density of states (DOS) of the CoS/Co-MOF composite shows a pronounced increase in electronic states near the Fermi level compared to pristine Co-MOF, reflecting enhanced metallic character upon heterostructure forma-

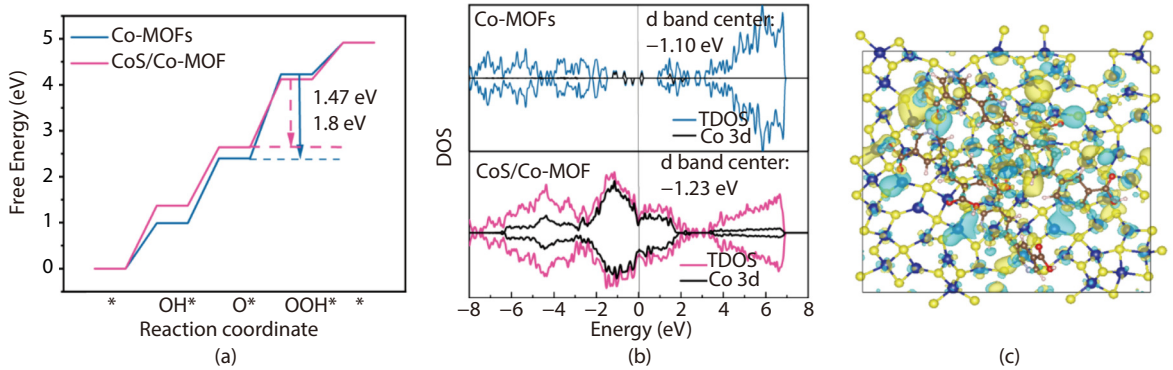

Fig. 8. (a) The corresponding free energy diagram for OER on Co-MOFs and CoS/Co-MOF composite, (b) the charge density difference of Co-MOFs and CoS/Co-MOF composite, and calculated DOS of Co-MOFs and CoS/Co-MOF composite, and (c) atomic structure model of the CoS/Co-MOF heterojunction interface.

tion. This improvement in electronic conductivity directly accounts for the experimentally observed low Tafel slope of 74.74 mV dec^{-1}. The reduced Tafel slope provides compelling evidence that the rate-determining step has shifted from adsorption-limited to a more facile charge-transfer process. Furthermore, the computed free-energy barriers align closely with the experimental overpotential of 327 mV required to reach 100 mA cm^{-2}, confirming the reliability of our theoretical model. Charge-density difference analysis reveals substantial electron redistribution at the CoS/Co-MOF interface, with electrons accumulating on the MOF side (Fig. S12). This interfacial electron transfer establishes a built-in electric field that facilitates directed charge transport, lowers interfacial resistance, and ultimately accelerates OER kinetics.

4. Conclusion

In summary, a 2D CoS/Co-MOF composite with reduced crystal diameters (~200 nm) was developed via a post-synthesis method. The 2D CoS/Co-MOF composite exhibits an ultrathin nanosheet structure with strong Co-S bonds and an S-S network. These structural characteristics enhance the electrical conductivity and structural stability of the sample. The resulting 2D CoS/Co-MOF composite electrocatalyst shows outstanding OER performance, with an overpotential of 327 mV at 100 mA cm^{-2}, a Tafel slope of 74.74 mV dec^{-1}, a high ECSA of 86.6 mF cm^{-2} and excellent stability (>20 h). The DFT calculations reveal that the Co-S bond optimizes the adsorption of oxygen intermediates and facilitates electron transfer by negatively shifting the d-band centre negatively to −1.23 eV, leading to stronger chemical bonding between the catalyst surface and adsorption intermediates. This optimizes the adsorption free energy and reduces the overpotential. These results were achieved through parameter optimization (TAA content: 450 mg, reaction temperature: 150°C, reaction time: 3 h). This work contributes to the ongoing development of efficient and durable electrocatalysts that are crucial for advancing sustainable hydrogen production technologies.

Acknowledgements

We gratefully acknowledge the financial support from the National Natural Science Foundation of China (22008032 and 12105048), the Guangdong Basic and Applied Basic Research Foundation (2024A1515030172), and the Guangdong Province Science and Technology Innovation Strategic Special Fund (Undergraduate Science and Technology Innovation Cultivation) (No. pdjh2025ak227）

Data availability statement

The data that support the findings of this study are available from the corresponding author upon reason able request.

Declaration of competing interest

The authors declare that they have no known competing financial interests or personal relationships that could have appeared to influence the work reported in this paper.

Electronic Supplementary Material (ESM)

The online version contains supplementary material available at https://doi.org/10.26599/ECS.2025.9600052.

References

[1] Peng M.; Ge Y. z.; Gao R.; Yang J.; Li A. w.; Xie Z. h.; Yu Q. l.; Zhang J.; Asakura H.; Zhang H.; Liu Z.; Zhang Q.; Deng J.; Zhou J. h.; Zhou W.; Hutchings G. J.Ma D. Thermal catalytic reforming for hydrogen production with zero CO_2 emission. *Science*, 2025; 387(6735).

[2] Rong C. l.; Huang X. y.; Arandiyan H.; Shao Z. p.; Wang Y.Chen Y. Advances in Oxygen Evolution Reaction Electrocatalysts via Direct Oxygen–Oxygen Radical Coupling Pathway. *Adv Mater*, 2025; 37(9).

[3] Wang Y.; Zhang M.; Liu Y.; Zheng Z.; Liu B.; Chen M.; Guan G.Yan K. Recent Advances on Transition-Metal-Based Layered Double Hydroxides Nanosheets for Electrocatalytic Energy Conversion. *Advanced Science*, 2023; 10(13).

[4] Gloag L.; Somerville S. V.; Gooding J. J.Tilley R. D. Co-catalytic metal–support interactions in single-atom electrocatalysts. *Nature Reviews Materials*, 2024; 9(3).

[5] Wang W.; Shan Q.; Xu J.; Li H.; Wang Y.; Hao R.; Wan X.; Zhao C.Wang W. Theoretical design rules for the reconstruction of transition metal sulfides during oxygen evolution reactions. *Journal of Energy Chemistry*, 2026; 112.

[6] Yuan S.; Zhang P.; Zhang L.; Garcia-Esparza A. T.; Sokaras D.; Qin J.-S.; Feng L.; Day G. S.; Chen W.; Drake H. F.; Elumalai P.; Madrahimov S. T.; Sun D.Zhou H.-C. Exposed Equatorial Positions of Metal Centers via Sequential Ligand Elimination and Installation in MOFs. *Journal of the American Chemical Society*, 2018; 140(34).

[7] Xiang Y. l.; Wei S. s.; Wang T. x.; Li H.; Luo Y.; Shao B.; Wu N. y.; Su Y. j.; Jiang L. b. Huang J. *Transformation of metal-organic frameworks (MOFs) under different factors. Coord Chem Rev*, 2025, 523(1): 216263.

[8] Kong L. j.; Cheng M. r.; Huang H.; Pang J. d.; Liu S.; Xu Y. h. Bu X. *H. Metal-organic frameworks for advanced aqueous ion batteries and supercapacitors. EnergyChem*, 2022, 4(6): 100090.

[9] Yang W. l.; Wang J. Jian J. *k. Metal organic framework-based materials for metal-ion batteries. Energy Storage Mater*, 2024, 66: 103249.

[10] Huang J.; Zhou S.; Zhang S.; Wang L.; Wu X. T.; Zhu Q. L.Wen Y. Two-dimensional layered MOF nanosheets with multiple binding sites for selective detection and removal of Fe(III) ions %J Separation and Purification Technology. 2024; 336.

[11] Duan Y. h.; Chen D. h.; Zhang R. y.; Du Y. m.Wang L. Optimizing the coordination environment of active sites to enhance heterogeneous electrocatalytic performances. *Coord Chem Rev*, 2025; 522.

[12] yuan X. L.; lu W. Z.qi G. J. 2D MOFs and their derivatives for electrocatalytic applications: Recent advances and new challenges *Coord. Chem. Rev.*, 2022; 472.

[13] Anuj K.K. G. R., *Atomically Precise Electrocatalysts for Electrochemical Energy Applications*, Edited, Springer Nature Switzerland.

[14] Narciso J.; Ramos-Fernandez E. V.; Delgado-Marín J. J.; Affolter C. W.; Olsbye U.Redekop E. A. New route for the synthesis of Co-MOF from metal substrates. *Microporous Mesoporous Mater*, 2021; 324.

[15] Ali H. M.; Tyagi V. K.; Kazmi A. A.Ojha C. S. P. Biohythane production from organic fraction of municipal solid waste: Clean and green energy generation under circular economy framework %J International Journal of Hydrogen Energy. 2024; 95.

[16] Xu Y. q.; Zhang Q.; Wang N. n.; Huang L. j.; Zhang X.; Lin H. j.; Xu Y. c.; Chen J. r. Jiao Y. Quasi-FeCo-MOF/CoS amorphous Nanosheets: A stable and highly active catalyst for electrocatalytic water splitting and monosaccharide oxidation. *Chem Eng J*, 2024, 497: 154837.

[17] Sun K. x.; Xu B. y.; Wang L. q.; Hu M. z.; Tang Z. h.; Chen Y. x.; Yang Y. q.; Zhang Q. Lang J. h. Simple activation effect on the EC hy-

drolysis performance of MOF structure. *Appl Surf Sci*, 2024, 644: 158813.

[18] Lv D. m.; Su S. b.; Zhang S. f. Cai D. d. Heterostructured ultrafine metal oxides nanoparticles anchored on Co-MOF nanosheets obtained by partial pyrolysis for promoted oxygen evolution reaction. *J Alloys Compd*, 2022, 912: 165143.

[19] Góbi S.; Reva I.; Tarczay G. Fausto R. Amorphous and crystalline thioacetamide ice: infrared spectra as a probe for temperature and structure. *J Mol Struct*, 2020, 1220: 128719.

[20] Wu L. L.; Wang Q. S.; Li J.; Long Y.; Liu Y.; Song S. Y.Zhang H. J. Co_9S_8 nanoparticles-embedded N/S-codoped carbon nanofibers derived from metal-organic framework-wrapped CdS nanowires for efficient oxygen evolution reaction. *Small*, 2018; 14(20).

[21] Fu R.; Song H. q.; Liu X. j.; Zhang Y. q.; Xiao G. j.; Zou B.; Waterhouse G. I. N. Lu S. y. Disulfide crosslinking-induced aggregation: towards solid-state fluorescent carbon dots with vastly different emission colors†. *Chin J Chem*, 2023, 41(9): 1007.

[22] Ren Y.Xu Y. Three-dimensional graphene/metal-organic framework composites for electrochemical energy storage and conversion. *Chem Commun*, 2023; 59(43).

[23] Zhao M.; Li W.; Li J.; Hu W. Li C. M. Strong electronic interaction enhanced electrocatalysis of metal sulfide clusters embedded metal-organic framework ultrathin nanosheets toward highly efficient overall water splitting. *Adv Sci*, 2020, 7(20): 2001965

[24] Lin Y. f.; Chen G.; Wan H.; Chen F. s.; Liu X. h. Ma R. z. 2D freestanding nitrogen-doped Ni-Ni_3S_2@carbon nanoplates derived from metal–organic frameworks for enhanced oxygen evolution reaction. *Small*, 2019, 15(18): 1900348.

[25] Xia T.; Yoshii T.; Nomura K.; Wakabayashi K.; Pan Z. Z.; Ishii T.; Tanaka H.; Mashio T.; Miyawaki J.; Otomo T.; Ikeda K.; Sato Y.; Terauchi M.; Kyotani T.Nishihara H. Chemistry of zipping reactions in mesoporous carbon consisting of minimally stacked graphene layers. *Chem Sci*, 2023; 14(32).

[26] Luo X. h.; Zhou Q. l.; Du S.; Li J.; Zhong J. w.; Deng X. l. Liu Y. l. Porous Co_9S_8/nitrogen, sulfur-doped carbon@Mo_2C dual catalyst for efficient water splitting. *ACS Appl Mater Interfaces*, 2018, 10(26): 22291.

[27] Yao C.; Wang Q.; Peng C. y.; Wang R. c.; Liu J. l.; Tsidaeva N. Wang W. MOF-derived CoS2/WS2 electrocatalysts with sulfurized interface for high-efficiency hydrogen evolution reaction: Synthesis, characterization and DFT calculations. *Chem Eng J*, 2024, 479: 147924.

[28] Yang Y.; Zeng R.; Xiong Y.; DiSalvo F. J. Abruña H. D. Cobalt-based nitride-core oxide-shell oxygen reduction electrocatalysts. *J Am Chem Soc*, 2019, 141(49): 19241.

[29] Chen W.; Wang Z.; Huang Z.; Xie W.; Zhao J.; Xiao Y.; Lei S.; Huang B. Cheng B. Mixed-dimensional van der Waals heterostructure of Bi2S3 nanorods and SnS2 nanosheets bridged with N-doped carbon interlayer for enhanced sodium-ion batteries. *Energy Storage Materials*, 2024, 73: 103880.

[30] Liu C.; Zhang Y.; Wu J.; Dai H.; Ma C.; Zhang Q. Zou Z. Ag-Pd alloy decorated ZnIn2S4 microspheres with optimal Schottky barrier height for boosting visible-light-driven hydrogen evolution. *Journal of Materials Science & Technology*, 2022, 114: 81.

[31] Tang Y.; Yuan Y.; Mo Y.; Tang H.; Wei M.; Zhou H.; Sheng T.; Li C.; Sun Y.Wei X. CoN//Co9S8 co-embedded in reduced graphene oxide as catalyst for catalytic conversion of polysulfides. *Materials Today Physics*, 2024; 46.

[32] Wang D.; Tian L. y.; Huang J. y.; Li D. w.; Liu J. y.; Xu Y.; Ke H. z.Wei Q. f. "One for two" strategy to prepare MOF-derived $NiCo_2S_4$ nanorods grown on carbon cloth for high-performance asymmetric supercapacitors and efficient oxygen evolution reaction. *Electrochim Acta*, 2020; 334: 135636.

[33] Yang L. f.; Zhang L.; Xu G. c.; Ma X.; Wang W. w.; Song H. j.Jia D. z. Metal-organic-framework-derived hollow CoS_x@MoS_2 microcubes as superior bifunctional electrocatalysts for hydrogen evolution and oxygen evolution reactions. *ACS Sustainable Chem Eng*, 2018; 6(10): 12961.

[34] Zhao C. X.; Liu J. N.; Wang C.; Wang J.; Song L.; Li B. Q. Zhang Q. An anionic regulation mechanism for the structural reconstruction of sulfide electrocatalysts under oxygen evolution conditions. *Energy Environ Sci*, 2022, 15(8): 3257.

[35] Chen Q. m.; Zhang Q. c.; Chen B.; Zhang J. h.; Peng W. c.; Li Y. Fan X. b. Enhanced long-term performance of sulfides in oxygen evolution reaction by sulfate ion-assisted strategy. *Adv Funct Mater*, 2024, 34(44): 2406233.

[36] Zhang Y.; Ma Y.; Yu J.; Li C.; Arbiol J.; Wang X.; Jian N.; Ge H.; Li L.; Cabot A. Li J. High-spin state electron configuration in Mn-doped Ni3Se4 for efficient methanol oxidation. *Journal of Energy Chemistry*, 2026, 112: 720.

[37] Chen S.; Huang H.; Jiang P.; Yang K.; Diao J.; Gong S.; Liu S.; Huang M.; Wang H.Chen Q. Mn-Doped RuO2 Nanocrystals as Highly Active Electrocatalysts for Enhanced Oxygen Evolution in Acidic Media. *ACS Catalysis*, 2020; 10(2).

[38] Lee G. Kim J. Effective tri-metal and dual-doped catalyst for oxygen evolution reaction: Amorphous Co-Mn-Ni-P-B-O nanoparticles. *Applied Surface Science*, 2022, 591: 153171.

[39] Review for "Oxygen spillover from RuO2 to MoO3 enhances activity and durability of RuO2 for acidic oxygen evolution". 2024.

[40] You B.; Tang M. T.; Tsai C.; Abild-Pedersen F.; Zheng X.Li H. Enhancing Electrocatalytic Water Splitting by Strain Engineering. *Advanced Materials*, 2019; 31(17).

[41] Zhang Z.; Li S.; Bu X.; Dai Y.; Wang J.; Bao X. Wang T. Hollow ZIF-67 derived porous cobalt sulfide as an efficient bifunctional electrocatalyst for overall water splitting. *New J Chem*, 2021, 45(37): 17313.

[42] Du J.; Wang R.; Lv Y. R.; Wei Y. L.Zang S. Q. One-step MOF-derived Co/Co_9S_8 nanoparticles embedded in nitrogen, sulfur and oxygen ternary-doped porous carbon: an efficient electrocatalyst for overall water splitting. *Chem Commun*, 2019; 55(22): 3203.

[43] Deng L. c.; Yang Z. x.; Li R.; Chen B. l.; Jia Q. l.; Zhu Y. q. Xia Y. d. Graphene-reinforced metal-organic frameworks derived cobalt sulfide/carbon nanocomposites as efficient multifunctional electrocatalysts. *Front Chem Sci Eng*, 2021, 15(6): 1487.

[44] Zou H.; He B.; Kuang P.; Yu J.Fan K. Metal-organic framework-derived nickel-cobalt sulfide on ultrathin MXene nanosheets for electrocatalytic oxygen evolution. *ACS Appl Mater Interfaces*, 2018; 10(26).

[45] Sun F. x.; Zhu S.; Liu Z. x.; Liu C.; Jiang K. z.; Zhang Y. y.; Chen B. Zheng S. j. Data-driven design of metal oxide electrocatalysts with low tafel slope in oxygen evolution reaction. *J Alloys Compd*, 2025, 1031: 180964.

[46] Wu B.; Gong S.; Lin Y. c.; Li T.; Chen A. y.; Zhao M. y.; Zhang Q. j. Chen L. A unique NiOOH@FeOOH heteroarchitecture for enhanced oxygen evolution in saline water. *Adv Mater*, 2022, 34(43): 2108619.

[47] Xu H. l.; Jiang L.; Yuan A. q.; Lei Y.; Wei Z. k.; Wang Y. c. Lei J. x. Thermally-stable, solid-solid phase change materials based on dynamic metal-ligand coordination for efficient thermal energy storage. *Chem Eng J*, 2021, 421: 129833.

[48] Cushing B. L.; Kolesnichenko V. L.O'Connor C. J. Recent advances in the liquid-phase syntheses of inorganic nanoparticles. *Chem Rev*, 2004; 104(9).

[49] Guan W.; Zhang L.; Wang P.; Wang Y.; Wang H. Y.; Dong X. C.; Meng M.; Sui L.; Gan Z. X.; Dong L. F.Yu L. Y. Highly Efficient Photocatalytic Hydrogen Evolution over Mo-Doped ZnIn(2)S(4) with Sulfur Vacancies. *Nanomater*, 2022; 12(22).

[50] Wang C. l.; Sawicki M.; Kaduk J. A. Shaw L. L. Roles of Processing, Structural Defects and Ionic Conductivity in the Electrochemical Performance of Na3MnCO3PO4Cathode Material. *J Electrochem Soc*, 2015, 162(8): A1601.